

pubs.acs.org/journal/apchd5 Article

# Influence of Laser Intensity and Location of the Fermi Level on Tunneling Processes for High-Harmonic Generation in Arrayed **Semiconducting Carbon Nanotubes**

Hiroyuki Nishidome, Mikito Omoto, Kohei Nagai, Kento Uchida, Yuta Murakami, Junko Eda, Hitomi Okubo, Kan Ueji, Yohei Yomogida, Junichiro Kono, Koichiro Tanaka, and Kazuhiro Yanagi\*



Cite This: ACS Photonics 2024, 11, 171-179



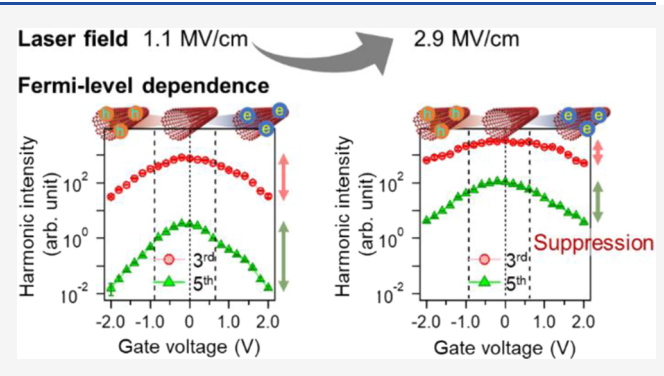
**ACCESS** I

III Metrics & More

Article Recommendations

Supporting Information

ABSTRACT: Recent advancement in high-power mid-infrared lasers has facilitated the investigation of extreme nonlinear optical phenomena in solids, which exhibit unconventional behaviors owing to strong light-matter interactions. High-harmonic generation (HHG) is a typical phenomenon that generates harmonics through nonperturbative processes. Herein, the strong laser field tunnels the charged particles from the valence to the conduction band and induces their carrier motion along the band, and then their motion generates high harmonics. In this study, we demonstrate that both the location of the Fermi level and the intensity of the laser field significantly affect the tunneling process in semiconducting carbon nanotubes through experimental



measurements and theoretical calculations. Additionally, on- or off-tunneling can determine the nonperturbative or perturbative harmonic generation processes, respectively, and this crossover can be observed owing to the shift in the gate voltage. Tuning the Fermi level and laser intensity is crucial for manipulating the tunneling process, carrier oscillations, and harmonic generation mechanisms. The results provide further insights into the nonlinear optical processes of semiconductors and pave the way for precisely controlling HHG in solids by using a static electric field.

KEYWORDS: high-harmonic generation, single-walled carbon nanotubes, electrolyte gating, extreme nonlinear optics, nonperturbative regime

## INTRODUCTION

High-harmonic generation (HHG), which generates multiple harmonics through strong light-matter interactions, is an extreme nonlinear optical phenomenon. 1-6 Owing to its nonperturbative characteristics, the relationships between the nth-harmonic and laser intensities  $I_L$  disobey the conventional nonlinear optical process  $\propto I_L^n$ . HHG was first observed in gaseous media and attracted attention because of its various remarkable applications, such as X-ray generation, attosecond pulse generation,<sup>8-10</sup> and tomography.<sup>11</sup> To this end, techniques required to control HHG features, such as the maximum harmonic order and high-harmonic intensity, have been developed. For instance, these HHG characteristics have been modulated by varying the laser intensity, 22 excitation wavelength, <sup>13</sup> polarization, <sup>14</sup> duration, <sup>15</sup> and chirp. <sup>16</sup> HHG in gaseous media has been influenced by the excitation laser parameters. Recently, HHG has been observed in various crystalline solids owing to recent advancement in intense midinfrared lasers. 17 HHG in solids functions as a probe for various essential physical parameters, such as the distribution of valence electrons, <sup>18</sup> band dispersion, <sup>19,20</sup> and topology, <sup>2</sup>

and has been investigated in one- or two-dimensional materials in both experimental and theoretical aspects. 22-32 In addition, it can be used for extreme UV sources<sup>33</sup> and ultrafast optoelectronics, 29-31,34 and thus, HHG has great potential for next-generation optoelectronic science and technologies. Numerous approaches have been proposed to control HHG in solids by varying the excitation laser parameters 17,24,35 and characteristics of the solid, such as the nanostructure, <sup>27</sup> crystal orientation, 17,36 electronic phase, 37-39 and electronic structure. 25,29,40 Using semiconductor device techniques, researchers have recently controlled HHG by applying a static electric field, such as by tuning the location of Fermi level  $E_{\rm F}^{29-31}$  and inversion symmetry.<sup>34</sup> These techniques have paved the way for control of the intensities and modes of HHG through the

Received: September 1, 2023 Revised: November 9, 2023 Accepted: November 9, 2023 Published: November 27, 2023





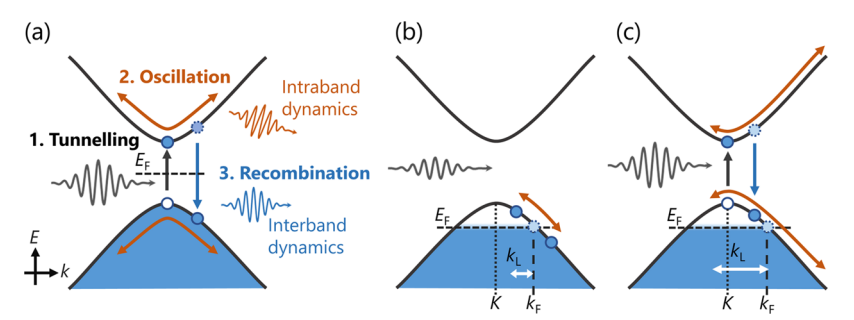


Figure 1. Mechanism for high-harmonic generation in semiconductors. (a) Illustration of HHG in semiconductors through tunneling of electrons from the valence to the conduction band (black arrow), carrier oscillation along the band (orange arrows), and their recombination (blue arrow). (b, c) Electron dynamics for hole-doped samples with weak (b) and strong (c) laser intensities.  $k_L = eF_L/\hbar\omega_L$  is the width of electron oscillations by the laser field (white arrows) in semiconducting carbon nanotubes, wherein the tunneling is only possible near the K-point. The dashed line shows the position of the Fermi level ( $E_F$ ) and Fermi wavenumber ( $k_F$ ). The dotted line shows the top of the valence band (or bottom of the conduction band) (k = K). When  $k_F > k_L$  (b), the electrons with  $|k| \ge k_F$  cannot approach the K-point and tunnel. Contrastingly, when  $k_F \le k_L$  (c), the electrons with  $k_F \le |k| \le k_L$  approach K, tunnel efficiently, and their motion is similar to that in panel (a).

electric field effect. However, in the previous studies on the relationships between HHG and  $E_{\rm F}$ ,  $^{29-31}$  the influence of the laser intensity, i.e., laser-field amplitude  $F_{\rm L}$ , on the HHG has been ignored, although  $F_{\rm L}$  significantly affects HHG processes. In this study, we demonstrate that the location of both  $E_{\rm F}$  and  $F_{\rm L}$  plays a key role in generating mechanisms, particularly the tunneling process, for high harmonics in semiconducting single-walled carbon nanotubes (SWCNTs). We found that combining the two parameters affects the system's tunneling process, which is crucial for nonperturbative HHG, significantly influences the HHG yield, and determines the nonperturbative or perturbative generation mechanisms.

First, the influence of  $E_{\rm F}$  and  $F_{\rm L}$  on the tunneling processes for HHG in semiconducting SWCNTs is briefly described (Figure 1). The HHG process in semiconductors whose band gap energy is larger than the photon energy of excitation laser pulse is explained by the following three-step processes.<sup>3–5</sup> Figure 1a shows the dynamics of electrons and holes in the lowest conduction and highest valence band during HHG. First, an intense laser field induces the tunneling of electrons from the top of the valence band to the bottom of the conduction band. Second, the laser field drives the tunneled carriers and oscillates them along the band, thereby inducing a nonlinear intraband current and radiating the high harmonics. Finally, the driven carriers recombine and emit the high harmonics. (We note that interband transitions can be also described by multiphoton excitation, depending on the laserfield strength and frequency.41 However, typically, HHG experiments, including the present study, fall into the tunneling regime; see the Discussion section for details.) Figure 1b,c shows the influence of the location of  $E_{\rm F}$  and the amount of  $F_{\rm L}$ on the tunneling processes. In semiconducting SWCNTs, the tunneling of electrons (or holes) at the top of the valence band (or the bottom of the conduction band) is dominant because this position has the smallest gap and largest dipole moment (see Figure S1 in the Supporting Information (SI)). Herein, the wavenumber of the tunneling position is termed  $k \equiv K$ . When  $E_{\rm F}$  is located below the band edge, the electrons in the valence band are initially driven to the K-point by the laser electric field to be tunneled into the conduction band. Therefore, the tunneling of electrons depends on the location of  $E_{\rm F}$  and the amount of  $F_{\rm L}$ . Using the laser light field of angular frequency  $\omega_{\rm L}$ , the electrons at  $E_{\rm F}$  can oscillate in kspace along the band with the center at the Fermi wavenumber

 $(k_{\rm F})$  and width of  $k_{\rm L} \bigg( = \frac{eF_{\rm L}}{\hbar\omega_{\rm L}} \bigg)$  based on the acceleration theorem (see eq (S26) in the SI). Thus, for  $k_{\rm F} > k_{\rm L}$  (Figure 1b), a majority of the electrons cannot tunnel, and HHG is significantly reduced (tunneling off). However, for  $k_{\rm F} \leq k_{\rm L}$  (Figure 1c), many of the electrons approach K, the carriers can efficiently tunnel between the band gap, and the tunneling electrons effectively emit high harmonics because of the aforementioned three-step mechanisms (tunneling on). Therefore, the tunneling on or off for HHG can be controlled not only by  $E_{\rm F}$  or  $F_{\rm L}$  but also by tuning "both" the  $E_{\rm F}$  and  $F_{\rm L}$ .

To clarify these characteristics, HHG in semiconducting SWCNTs was investigated by varying the gate voltages and laser intensities. An aligned film was prepared using the semiconducting SWCNTs with a diameter of 1.4 nm (the thickness of the film was 18 nm, and band gap energy  $E_{\rm g}$  was 0.7 eV)<sup>42–47</sup> and fabricated a side-gate device with an ion gel (shown in Figure 2a) to inject electrons or holes by varying the gate voltage  $V_{\rm G}^{29,48-51}$  (the details are given in the Methods section, Figures S2-S5, and Tables S1 and S2 in the SI). For the HHG measurements, intense mid-infrared (MIR) light was generated at 4.8 µm (central energy: 0.26 eV; pulse duration: 60 fs), and its intensity and polarization were tuned by combining a pair of wire-grid polarizers and a liquid crystal retarder. The semiconducting SWCNTs showed maximum high-harmonic intensity with an MIR polarization parallel to the SWCNT axis, reflecting their one-dimensional features (the polarization dependence is given in Figure S5 in the SI). Thus, the MIR polarization was set parallel to the SWCNT axis. The high-harmonic signals generated from the sample were detected using an InGaAs line detector (for the third harmonic), a Si charge-coupled device (for the fifth and higher harmonics), and a spectrometer.

# RESULTS

The influences of  $E_{\rm F}$  and  $F_{\rm L}$  on the intensities of high harmonics were discussed experimentally. Figure 2b,c indicates HHG as a function of  $V_{\rm G}$  at  $F_{\rm L}=1.1$  MV/cm. The transport characteristics indicate typical semiconducting-type behavior, including clear ambipolar behavior and an on/off ratio of  $10^3$  (the bottom graph in Figure 2c). As shown in Figure 2b, the HHG spectra are described as the shift of  $V_{\rm G}$  from the charge neutral point (CNP) corresponding to the voltage at which the sample current  $I_{\rm SD}$  is minimum. The spectra indicate the

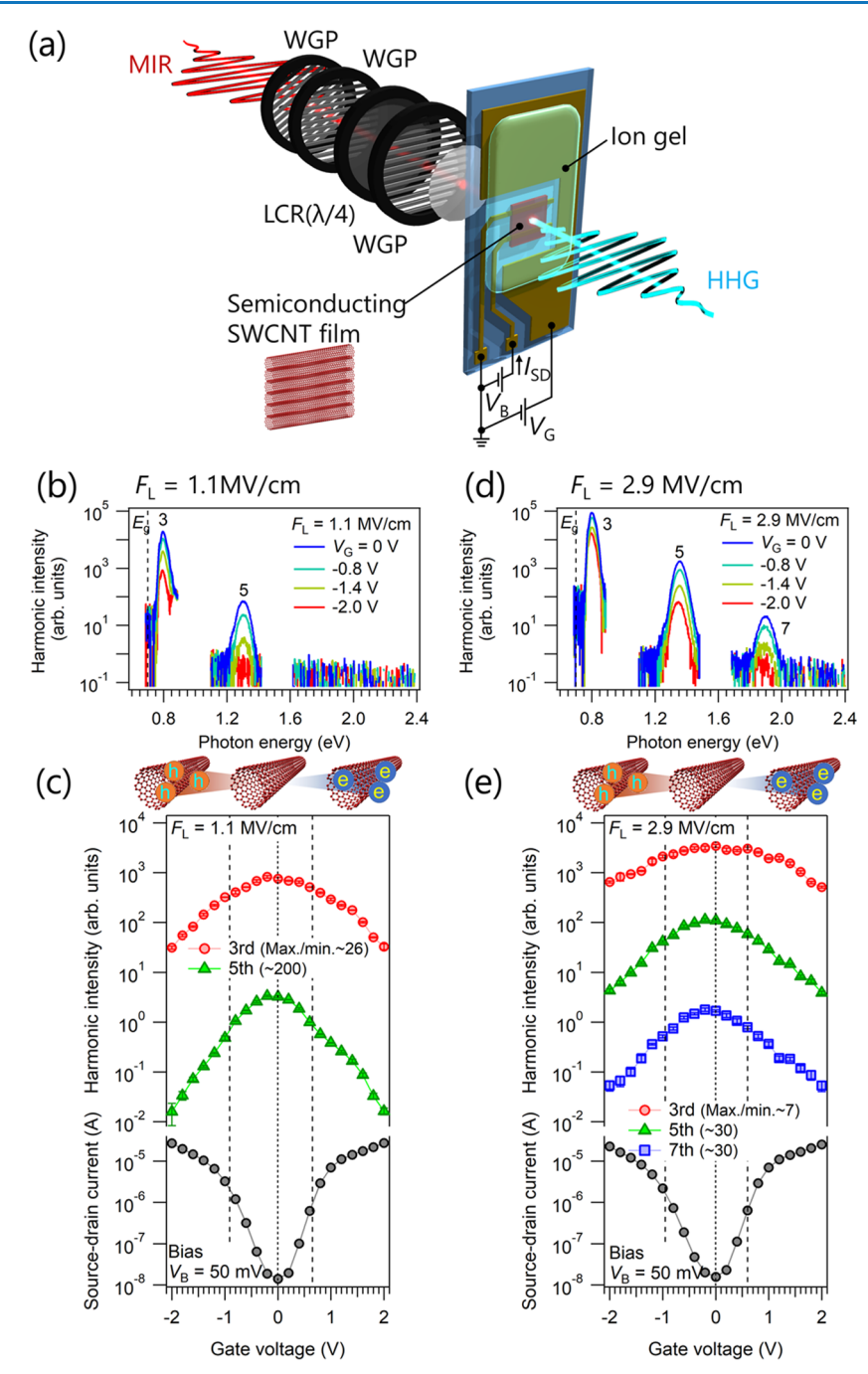


Figure 2. Variation in HHG by tuning the Fermi level and laser-field amplitude. (a) Experimental setup and device structure. WGP, wire-grid polarizer and LCR, liquid crystal retarder. The Fermi level of the semiconducting SWCNT film was tuned by using the electrolyte gating method through gate voltage  $V_G$ .  $V_B$  is the bias voltage. (b, d) High-harmonic spectra with a negative gate voltage shift corresponding to hole injection at  $F_L$  = 1.1 MV/cm (b) and 2.9 MV/cm (d). (c, e) High-harmonic intensity (top) and sample current  $I_{SD}$  (bottom) as a function of the gate voltage at 1.1 MV/cm (c) and 2.9 MV/cm (e). The error bars represent the standard deviations, and the dashed lines indicate the locations of the band edges.

appearance of the third and fifth harmonics, and the high-harmonic intensities decreased with a negative shift of  $V_{\rm G}$ , indicating hole doping. Similar spectral behaviors were observed with the positive shift of  $V_{\rm G}$ , i.e., electron doping, as shown in Figure S6 in the SI, in agreement with symmetrical valence and conduction band structures at the K-point. Notably, the photon energy of the third harmonic (0.78 eV) is greater than  $E_{\rm g}=0.7$  eV (the dashed line in Figure 2b,d). Hence, the suppression of the intensities of higher-order harmonics compared to the third harmonic is consistent with

the outcomes of our previous study. The high-harmonic intensities decrease owing to the positive and negative shifts of  $V_{\rm G}$ . Furthermore, the graph contains two characteristic regions. In the first region, the high-harmonic intensity is approximately constant with respect to the variation in  $V_{\rm G}$  (-1.0 V <  $V_{\rm G}$  < 0.6 V). The flat region coincides with the off-state region of the  $I_{\rm SD}$  transfer curve; hence,  $E_{\rm F}$  is located within the gap (see Figure S7 and the sample capacitance in Figure S8 in the SI). In the second region, the intensity decreases significantly with respect to the variation in  $V_{\rm G}$  ( $V_{\rm G}$  < - 1.0 V,  $V_{\rm G}$  > 0.6 V). Herein,  $E_{\rm F}$ 

should be located below the valence or above the conduction band. The  $I_{\rm max}/I_{\rm min}$  ratios of the third and fifth harmonic intensities were ~26 and ~200, respectively, where  $I_{\rm max}$  and  $I_{\rm min}$  are the maximum and minimum intensity of each harmonic order within  $-2~{\rm V} \le V_{\rm G} \le 2~{\rm V}$ , respectively.

Furthermore, the same measurement was performed at  $F_{\rm L}=2.9~{\rm MV/cm}$  (Figure 2d,e). At 2.9 MV/cm, as with the case of 1.1 MV/cm, all high-harmonic intensities decreased, but the reductions were significantly suppressed compared with the case at 1.1 MV/cm. The  $I_{\rm max}/I_{\rm min}$  ratio of the third harmonic was 7, and that of the fifth harmonic was ~30. Table 1

Table 1. Maximum and Minimum HHG Intensity Ratios  $(I_{\text{max}}/I_{\text{min}})$  from Carrier Injection at Various Laser Amplitudes (Thin Sample)

$F_{\rm L}$ (MV/cm)	1.1	1.7	2.2	2.9
$I_{\rm max}/I_{\rm min}$ for third harmonic	26	12	8	7
$I_{\rm max}/I_{\rm min}$ for fifth harmonic	200	70	50	30

summarizes the  $I_{\rm max}/I_{\rm min}$  for the third and fifth harmonics at four different  $F_{\rm L}$ 's, and the results at 1.7 and 2.2 MV/cm are shown in Figure S9 in the SI. Evidently, large  $F_{\rm L}$  values reduced the  $I_{\rm max}/I_{\rm min}$  ratios of all high harmonics. Similar measurements were performed using another aligned SWCNT film, and similar trends were observed (see Figures S10 and Table S3 in the SI). As shown here, HHG strongly depends on the location of  $E_{\rm F}$  (HHG- $V_{\rm G}$  relation), and remarkably, the line shape of the HHG- $V_{\rm G}$  relation significantly depends on the laser intensity, which is explained by using the following theoretical calculation, along with the influence of the tunneling process on the plots.

# DISCUSSION

**Calculation Model and Its Validity.** Herein, the model used for calculating the HHG spectra as a function of  $E_{\rm F}$  and  $F_{\rm L}$  is discussed (the details are provided in the SI). An effective two-band model has been assumed for the semiconducting SWCNT with a diameter of 1.4 nm, including the lowest conduction and highest valence bands with  $E_{\rm g}=0.6$  eV and the Dirac band structures. While irradiating the system with a 60 fs MIR laser pulse, the time evolutions of the two types of currents, i.e., the interband polarization and intraband current, were evaluated using the semiconductor Bloch equation.  $^{32,53-55}$  The Fermi–Dirac distribution was implemented using  $E_{\rm F}$  as the initial state, which was systematically varied. If

 $E_{\rm F}$  was situated in the middle of the band gap, then its value was set to zero. Thereafter, the high-harmonic spectra were calculated by using the Fourier transform of the time evolution of currents. To reproduce the behaviors of the experimentally observed third and fifth harmonic intensities, the relaxation time  $T_1$  of the population and dephasing time  $T_2$  were set to be 22 and 4.4 fs, respectively.

The calculated relationships among  $E_F$ ,  $F_L$ , and HHG are discussed. Figure 3a,b shows the calculated intensities of the third and fifth harmonics as functions of  $E_F$  at  $F_L = 1$  and 3 MV/cm, respectively. The details of the calculated HHG spectra are shown in Figure S11 in the SI. Evidently, the calculation results qualitatively reproduce the following two characteristics: (1) the HHG vs  $E_F$  plot and (2) the influence of  $F_L$  on the line shapes of HHG vs  $E_F$  plots. For (1), the calculation reproduces the presence of the two regions, the constant and decreased high-harmonic intensities, with respect to the variation in  $E_F$ . The results are consistent with the relationships between  $E_{\rm F}$ , band structures, and HHG in our previous work.<sup>24</sup> For (2), the calculated results indicate that the  $I_{\text{max}}/I_{\text{min}}$  ratios decrease with increasing  $F_{\text{L}}$ . Thereby, the calculation confirms that the line shape of the HHG-V<sub>G</sub> relation significantly depends on the laser intensity.

According to the definition suggested by ref 41, the interband transitions can be categorized using the following three concepts, multiphoton excitation, diabatic tunneling, and adiabatic tunneling, depending on the value of Keldysh parameters  $\gamma$ . When  $\gamma\gg 1$ , the process is described as the multiphoton excitation. When  $\gamma\sim 1$ , it is described as diabatic tunneling and when  $\gamma\ll 1$ , as adiabatic tunneling. In this study, the  $\gamma$  values are 2.4 and 0.8 for 1 and 3 MV/cm laser field, respectively (the details are given in the SI). Thus, according to this definition, the interband transitions in this study can be described as the diabatic tunneling. Therefore, we used the term of "tunneling" for the interband transition processes in this study. Next, we will discuss the details of the background of the influence of  $F_{\rm L}$  on the line shapes of HHG vs  $E_{\rm F}$  plots.

**Dynamics in** *k***-Space and Tunneling.** Figure 4 shows the oscillations of the laser electric field as a function of time at  $F_{\rm L}=1~{\rm MV/cm}$  (Figure 4a) and 3 MV/cm (Figure 4b) and the corresponding wave-packet motion of conduction electron density  $\rho_{\rm cc}(k_{\rm w}t)$  at  $E_{\rm F}=0~{\rm eV}$  (Figure 4c,d) and  $E_{\rm F}=-0.5~{\rm eV}$  (Figure 4e,f). Herein, the *K*-point was set to the point at  $k_{\rm x}=0$ . The colors indicate the carrier density in  $\rho_{\rm cc}(k_{\rm w}t)$ , and the time evolution of the nondiagonal term  $\rho_{\rm cv}(k_{\rm w}t)$  is depicted in

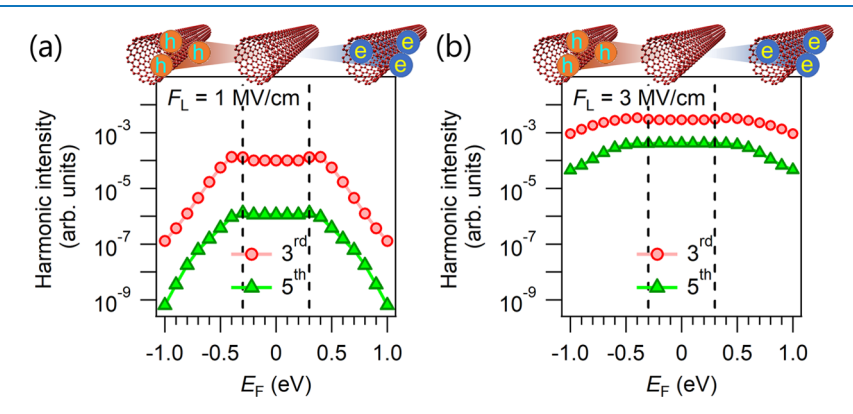


Figure 3. Behavior of the calculated high harmonics. Calculated intensities of the third and fifth harmonics as a function of the Fermi level  $E_{\rm F}$  at laser amplitudes  $F_{\rm L} = 1$  (a) and 3 MV/cm (b). Dashed lines indicate the locations of the top valence band and bottom conduction band.

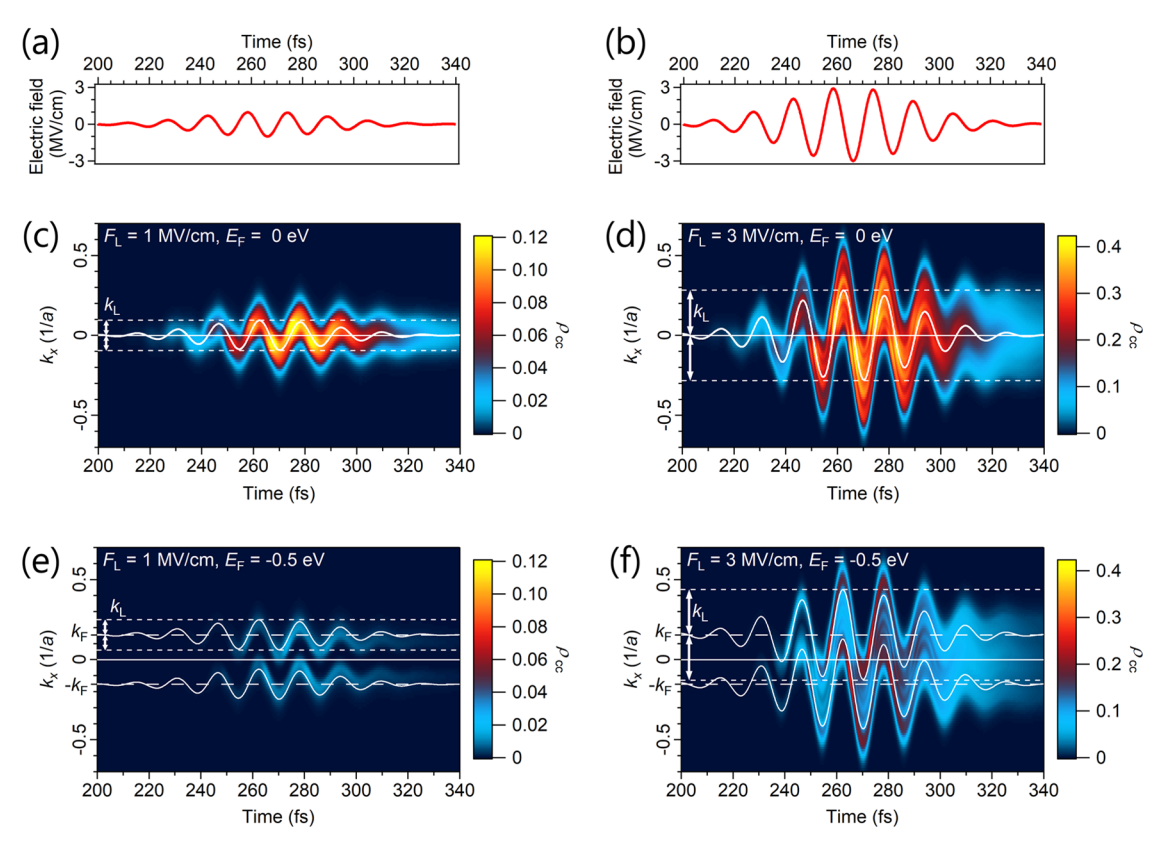


Figure 4. Wave-packet motions of electrons in the conduction band. (a, b) Electric laser-field profile used for calculating the laser amplitudes at  $F_{\rm L}$  = 1 MV/cm (a) and 3 MV/cm (b). (c-f) Mapping the temporal evolution of electron density in the conduction band,  $\rho_{\rm cc}$  for  $F_{\rm L}$  = 1 (c, e) and 3 MV/cm (d, f) with Fermi levels  $E_{\rm F}$  = 0 (c, d) and -0.5 eV (e, f). The mapping color indicates the tunneled electrons in the band. The dashed lines depict the maximum amplitude of the oscillating electron wave packet in k-space,  $k_{\rm L}$  = e $F_{\rm L}/\hbar\omega_{\rm L}$ . The bottom of the conduction band is set at the origin  $k_x$  = 0 and depicted as a white line in panels (c-f). The white curves are  $k_x$  = -e $A_{\rm L}(t)/\hbar \pm k_{\rm F}$ , where  $A_{\rm L}(t)$  is the vector potential of the laser field.

Figure S13 in the SI. First, the time evolution of  $\rho_{cc}(k_{x}t)$  at  $E_{\rm F}=0$  eV with different  $F_{\rm L}$  values is discussed. The carriers oscillate around the K-point and oscillating width of  $k_{\rm L}$ . The dynamics of  $\rho_{cc}(k_{x}t)$  at  $F_{\rm L}=1$  MV/cm (Figure 4c) indicate that electrons can tunnel from the valence to the conduction band at the K-point and generate high harmonics. Compared with  $\rho_{cc}(k_{x}t)$  at  $F_{\rm L}=1$  and 3 MV/cm (Figure 4c,d, respectively), the increase in  $F_{\rm L}$  influences the range of the tunneling electrons and their oscillating range in k-space.

At  $E_{\rm F} = -0.5$  eV, valence electrons oscillate around the Fermi wavenumber  $k_F$  by the laser field (white dashed line). Hence, at  $F_L = 1 \text{ MV/cm}$  (Figure 4e)  $(k_F > k_L)$ , the majority of electrons cannot approach the K-point, indicating a very low tunneling probability (as shown in Figure 1b). However, at  $F_{\rm L}$ = 3 MV/cm (Figure 4f) ( $k_{\rm F} < k_{\rm L}$ ), the oscillation of the laserdriven electrons approaches the K-point, indicating that tunneling is possible for the electrons near  $\pm k_F$  (as shown in Figure 1c). The number of tunneled carriers at  $E_{\rm F} = -0.5$  eV is small compared with the case at  $E_F = 0$  eV, and thus, the HH intensity at  $E_{\rm F} = -0.5$  eV becomes small compared with that at  $E_{\rm F}$  = 0 eV. However, when  $F_{\rm L}$  is strong enough to satisfy  $k_{\rm F}$  <  $k_{\rm L}$ , the electrons tunneled at  $E_{\rm F} = -0.5$  eV can generate high harmonics with an intensity comparable to the high harmonics at  $E_{\rm F}$  = 0 eV; therefore, the reduction in the high-harmonic intensity with respect to the variation in  $E_{\rm F}$  is sufficiently suppressed. Hence, the increase in the laser intensity decreased the  $I_{\text{max}}/I_{\text{min}}$  ratios. These results indicate that tuning both  $E_{\text{F}}$ 

and  $F_L$  is crucial for controlling the tunneling process for HHG.

Crossover from the Nonperturbative to Perturbative **Process by Shifting V\_G.** The intraband dynamics of carriers contribute to HHG. However, when the carriers cannot traverse through the K-point in the 1D-Dirac band structure (tunneling-off condition), their velocities change negligibly; hence, the contribution of this mechanism to HHG is small.<sup>32,57,58</sup> Consequently, in the tunneling-off condition, the carrier cannot generate high harmonics through the recombination mechanism with tunneling and intraband mechanisms (the details of the relationships among the intensity of HHG,  $E_{\rm F}$ , and  $F_{\rm L}$  are shown in Figure S14 in the SI). In the absence of the tunneling processes and negligible interband mechanisms for HHG, the majority of high harmonics should be generated through multiple photon excitation processes described by using perturbative optical processes. This indicates a shift from the nonperturbative nonlinear process to perturbative process by tuning  $E_{\rm F}$  and  $F_{\rm L}$ . Thus, we investigate how the location of E<sub>F</sub> affects the relationships between the nth-harmonic intensity and laser intensity  $I_L$ . In Figure 5a, the calculated plot is depicted for the third-harmonic intensity as a function of laser intensity  $I_{\rm L}=\frac{1}{2}\sqrt{\frac{\epsilon_0}{\mu_0}}F_{\rm L}^2$  at  $E_{\rm F}=0$  and 0.6 eV. At  $E_{\rm F}=0$ , the value of the exponent n in  $\propto I_L^n$  varied from 1.5 to 3 as  $I_L$  decreased, indicating a transition from a nonperturbative to perturbative process. The transition intensity is denoted by a dashed line.

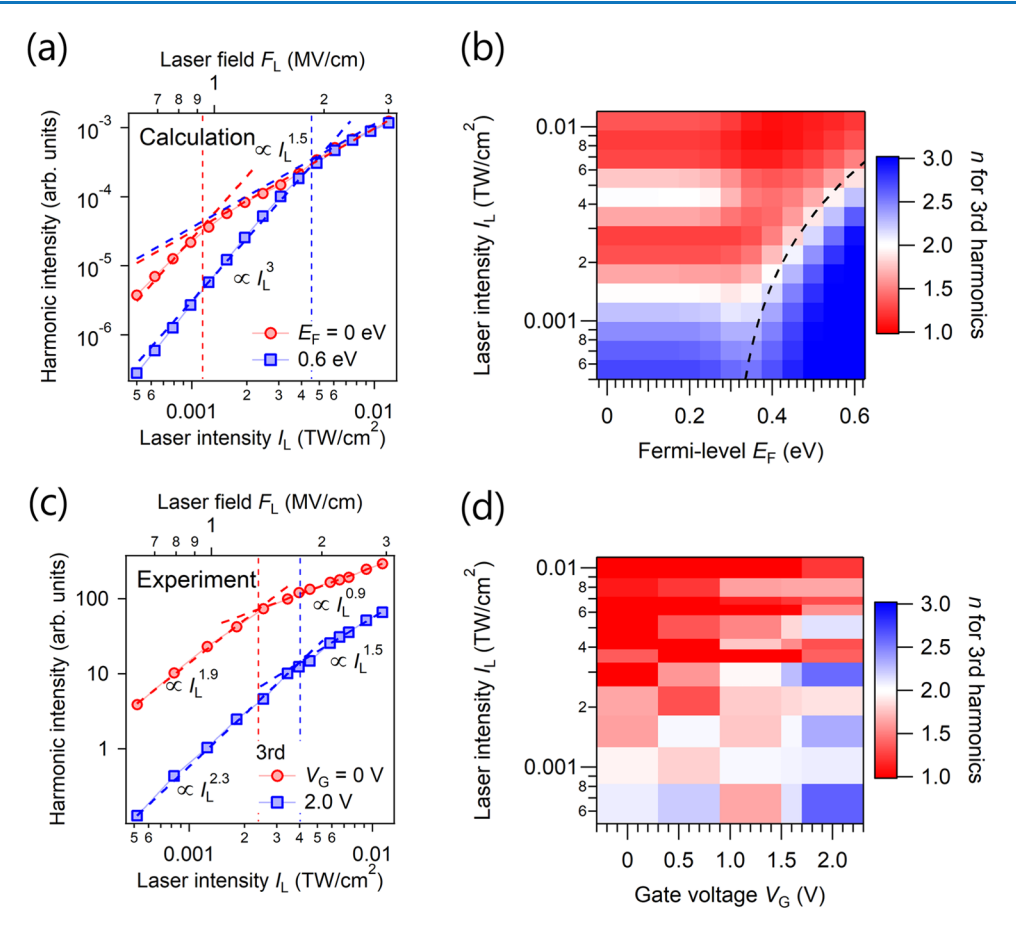


Figure 5. Crossover from the nonperturbative to the perturbative regime. (a) Calculated results for the relationships among the laser intensity  $I_L$  and third-harmonic intensity at  $E_F = 0$  and 0.6 eV. The red and blue dashed lines are the transition intensities distinguishing the small and large exponent n regions in  $\alpha I_L^n$ . (b) Calculated mapping describing the relationships among  $I_L$ ,  $E_F$ , and the value of exponent n in  $\alpha I_L^n$  for the third harmonics. Black dashed lines indicate the boundaries of  $k_F = k_L$  (see the SI). (c) Experimental relationships among  $I_L$  and third-harmonic intensity at  $V_G = 0$  and 2.0 V. (d) Mapping the relationships among  $I_L$  and the value of n for the third harmonics.

Based on the Keldysh parameter,<sup>56</sup> the electric field that induces tunneling is estimated to be 2.4 MV/cm (see the SI), which is within the calculation and measurement range, thereby validating the observed transition from nonperturbative to perturbative. Remarkably, at  $E_F = 0.6$  eV, the transition intensity increased. To understand the background in more detail, the calculated mapping of n as a function of  $I_L$  and  $E_F$ was plotted (Figure 5b) to indicate the two transitional features from nonperturbative to perturbative processes more clearly. The details of the calculations are depicted in the SI. The first is the conventional transition from nonperturbative to perturbative processes by decreasing the laser intensity, and the second is the transition owing to the shifting of  $E_F$ . In the conventional transition, when the laser intensity decreases, n changes from 1 to 3, indicating that the generation process shifts from nonperturbative to perturbative. Additionally, the calculation suggests that the location of  $E_F$  significantly influences the value of the exponentiation factor. The black dashed line indicates the tunneling threshold ( $k_{\rm F} = k_{\rm L}$ ) (see the SI). When  $k_F \leq k_L$ , the tunneling is possible wherein nbecomes less than 3 (the nonperturbative characteristics). In contrast, when  $k_F > k_L$ , tunneling is impossible wherein n becomes 3. Hence, the high harmonics are majorly generated through the perturbative process. The simulation results clearly predicted that a transition from the nonperturbative to the perturbative process would be observed by shifting  $F_L$  and  $E_F$ .

To verify the aforementioned calculation results, the thirdharmonic intensity was plotted as a function of  $I_L$  at  $V_G = 0$  and 2.0 V, as shown in Figure 5c. According to the capacitance measurements, here, we assume that  $E_F$  was located at around 0.6 eV at  $V_G$  = 2.0 V (see the SI). Although the value of the exponential factor does not precisely correspond to the values expected in the calculations, which might be caused by the inhomogeneity of semiconducting SWCNTs with different chiralities and the nonuniformity of laser intensity in the laser spot, a similar tendency can be observed as follows. The nvalues transitioned with respect to the variation in  $I_L$ , and the transition point shifted to the larger laser intensity owing to the shift in  $V_G$ . Figure 5d indicates the mapping of n values as a function of  $I_L$  and  $V_G$ , wherein n transitions from a small value to a large value as the laser intensity decreases at each gate voltage. Additionally, this transition was observed owing to the shift in  $V_{\rm G}$  for the same laser intensity, implying the crossover from nonperturbative to perturbative processes. The plot suggests that  $I_L$  and the shift in  $E_F$  influence the HHG mechanisms. Regarding the behaviors in other harmonics, like the fifth harmonic, we also observed similar features (Figure S16 in the SI).

# CONCLUSIONS

In this study, the importance of tuning both the location of the Femi level and laser intensity was established for controlling the generation processes of high harmonics. In the semiconducting SWCNTs, these two parameters influence the possibility of tunneling processes for HHG. Additionally, the combination of the two factors influences whether the high harmonics are primarily generated from the nonperturbative or perturbative nonlinear optical process. The results provide further insights into the nonlinear optical processes of semiconductors and open a way to control HHG in solids precisely with an electric field.

#### METHODS

**Device Preparation.** The semiconducting SWCNTs were prepared using the density-gradient sorting method from SWCNTs produced by the arc discharge method (Arc SO, Meijyo Nanocarbon Co.). 42-44 The optical absorption spectrum of the semiconducting SWCNTs is shown in Figure S2 in the SI, and the semiconducting purity is estimated to be more than 95%. 44 The aligned films were fabricated using the controlled vacuum filtration method. 45-47 The film thickness was 18 nm, and the  $E_{\rm g}$  was 0.7 eV, as estimated from the optical transition energy between the first valence and conduction bands. Details for evaluating the alignment film are provided in Figures S3-S5 and Tables S1 and S2 in the SI. The film was transferred onto a sapphire substrate (thickness:  $430 \pm 25 \mu m$ ) with Au (100 nm)/Ti (3 nm) electrodes.  $E_F$  of the semiconductor SWCNT films was tuned using the electrolyte gating method.<sup>29,48-51</sup> As shown in Figure 2a, a side-gate device was fabricated and an ion gel was used as the electrolyte to inject electrons or holes by shifting the gate voltage  $V_G$ . The ion gel was a mixture of EMIM-TFSI (Kanto Chemical Co.) and PS(5000)-PMMA(75,000)-PS(5000) in dichloromethane (the weight ratio was 7:1:270).

HHG Measurements. For the HHG measurements, a Tisapphire regenerative amplifier system (repetition rate: 1 kHz, center wavelength: 800 nm, pulse duration: 35 fs, pulse energy: 7 mJ) was used as the laser source. Intense mid-infrared (MIR) light with a 4.8  $\mu$ m wavelength (central energy: 0.26 eV, pulse duration: 60 fs) was generated using difference frequency mixing of signal and idler outputs from an optical parametric amplifier (TOPAS-C, Light Conversion). The chirp compensation windows are inserted to reduce the chirp, which is caused by the sapphire substrate of the device, the vacuum chamber window, and so on. The spot size of the MIR pulses was estimated to be 60  $\mu m$  (full width at half-maximum of intensity). The intensity and polarization of the MIR light were tuned by combining a pair of wire-grid polarizers and a liquid crystal retarder. MIR polarization was set parallel to the SWCNT axis based on the crystal orientation dependence of the HHG yield. To avoid degradation of the sample during measurement, the MIR light was focused on the side-gating device in the vacuum chamber ( $<10^{-3}$  Pa). The high-harmonic signals from the sample were detected using an InGaAs line detector (for third harmonics) and a Si charge-coupled device (for fifth and higher harmonics) equipped with a spectrometer.

When HHG was measured as a function of  $V_{\rm G}$ , the source-drain current  $I_{\rm SD}$  at a given  $V_{\rm G}$  was first checked at a bias voltage  $V_{\rm B}=50$  mV without laser irradiation, and then HHG was measured at the same  $V_{\rm G}$  and  $V_{\rm B}=0$  mV. We adjusted the laser intensities where we could confirm the returnability of HHG by the shift of  $V_{\rm G}$ , indicating no degradation during the measurements. Strong infrared driving of electrons sometimes causes the rise of the electronic temperature, resulting in thermal emission from the sample. We have observed such

broad luminescence in metals and semimetals.<sup>24,29</sup> However, in the case of semiconducting SWCNTs, such luminescence is negligibly small compared to the HH intensities.

Figure S17 in the SI shows the HH spectra from the sapphire substrate. The substrate generates the third harmonic, but its intensity is negligible compared to the signal from the sample, which is one-tenth smaller than that of SWCNTs. There are no fifth- or higher-order harmonics, even at  $F_{\rm L}=7.5$  MV/cm. In addition, we have not observed any change in HHG from the substrate and gel by the shift of  $V_{\rm G}$ .

#### ASSOCIATED CONTENT

# **Solution** Supporting Information

The Supporting Information is available free of charge at https://pubs.acs.org/doi/10.1021/acsphotonics.3c01244.

Structure of the band dispersion and dipole moment of semiconducting SWCNTs, evaluation of the samples (the optical absorption spectrum, atomic force microscopy (AFM) images, Raman signals, transfer characteristics, and their capacitance), additional HHG results, details of the calculation, comparison of the intraband and interband dynamics, and details of the analysis about the wave-packet motion of electrons, the mapping of the power dependence, and the intensity for tunneling (PDF)

#### AUTHOR INFORMATION

#### **Corresponding Author**

Kazuhiro Yanagi — Department of Physics, Tokyo Metropolitan University, Tokyo 192-0397, Japan; orcid.org/0000-0002-7609-1493; Email: yanagi-kazuhiro@tmu.ac.jp

#### Authors

Hiroyuki Nishidome — Department of Physics, Tokyo Metropolitan University, Tokyo 192-0397, Japan; ⊚ orcid.org/0009-0001-9053-2646

Mikito Omoto – Department of Physics, Tokyo Metropolitan University, Tokyo 192-0397, Japan

Kohei Nagai — Department of Physics, Kyoto University, Kyoto 606-8502, Japan

Kento Uchida – Department of Physics, Kyoto University, Kyoto 606-8502, Japan

Yuta Murakami — Center for Emergent Matter Science, RIKEN, Wako, Saitama 351-0198, Japan

**Junko Eda** – Department of Physics, Tokyo Metropolitan University, Tokyo 192-0397, Japan

Hitomi Okubo – Department of Physics, Tokyo Metropolitan University, Tokyo 192-0397, Japan

Kan Ueji – Department of Physics, Tokyo Metropolitan University, Tokyo 192-0397, Japan; orcid.org/0000-0003-1254-0699

Yohei Yomogida — Department of Physics, Tokyo Metropolitan University, Tokyo 192-0397, Japan; orcid.org/0000-0002-8569-6179

Junichiro Kono — Department of Electrical & Computer Engineering, Department of Physics & Astronomy, Department of Materials Science & NanoEngineering, and the Smalley-Curl Institute, Rice University, Houston 77005, United States; Occid.org/0000-0002-4195-0577

Koichiro Tanaka – Department of Physics, Kyoto University, Kyoto 606-8502, Japan; Institute for Integrated Cell-Material Sciences, Kyoto Universitys, Kyoto 606-8501, Japan

Complete contact information is available at: https://pubs.acs.org/10.1021/acsphotonics.3c01244

## **Author Contributions**

H.N., K.N., K.U., M.O., and K.Y. performed experiments and analyzed the experimental data. H.N., M.O., J.E., H.O., K.U., Y.Y., and J.K. prepared samples and devices. H.N., K.U., and Y.M. performed theoretical modeling and simulation. K.Y. and K.T. conceived and supervised the project. All authors contributed to the preparation of the manuscript.

#### Funding

H.N. acknowledges support from JSPS KAKENHI through Grant No. JP20J22225. K.U. is thankful for a Grant-in-Aid for Scientific Research (C) (Grant No. 22K03484) and Grant-in-Aid for Challenging Research (Pioneering) (Grant No. 22K18322). Y.M. acknowledges support from Grant-in-Aid for Scientific Research from JSPS, KAKENHI Grant Nos. JP20K14412 and JP21H05017, and JST CREST Grant No. JPMJCR1901. K.U. acknowledges support from the Shimadzu Science Foundation. K.T. acknowledges support from Grantin-Aid for Scientific Research (S) (Grant Nos. JP17H06124 and JP21H05017). J.K. acknowledges support from the Robert A. Welch Foundation (through Grant No. C-1509), the National Science Foundation (through Grant No. PIRE-2230727), and the Air Force Office of Scientific Research (through Grant No. FA9550-22-1-0382). K.Y. acknowledges support from JSPS KAKENHI, Grant Nos. JP17H06124, JP20H02573, JP21H05017, JP22H05469, and JP23H00259, and JST CREST through Grant No. JPMJCR17I5, Japan, and US-JAPAN PIRE collaboration, Grant No. JPJSJRP20221202, Japan, and Tokyo Metropolitan Government Advanced Research Grant Number (H31-1).

#### **Notes**

The authors declare no competing financial interest.

# ABBREVIATIONS

HHG, high-harmonic generation; SWCNTs, single-walled carbon nanotubes; MIR, mid-infrared

### REFERENCES

- (1) Corkum, P. B. Plasma perspective on strong field multiphoton ionization. *Phys. Rev. Lett.* **1993**, *71* (13), 1994–1997.
- (2) Lewenstein, M.; Balcou, P.; Ivanov, M. Y.; L'Huillier, A.; Corkum, P. B. Theory of high-harmonic generation by low-frequency laser fields. *Phys. Rev. A* **1994**, *49* (3), 2117–2132.
- (3) Vampa, G.; McDonald, C. R.; Orlando, G.; Klug, D. D.; Corkum, P. B.; Brabec, T. Theoretical analysis of high-harmonic generation in solids. *Phys. Rev. Lett.* **2014**, *113* (7), No. 073901.
- (4) Vampa, G.; McDonald, C. R.; Orlando, G.; Corkum, P. B.; Brabec, T. Semiclassical analysis of high harmonic generation in bulk crystals. *Phys. Rev. B* **2015**, *91* (6), No. 064302.
- (5) Ghimire, S.; Reis, D. A. High-harmonic generation from solids. *Nat. Phys.* **2019**, *15* (1), 10–16.
- (6) Chin, A. H.; Calderón, O. G.; Kono, J. Extreme Midinfrared Nonlinear Optics in Semiconductors. *Phys. Rev. Lett.* **2001**, *86* (15), 3292–3295.
- (7) Li, X. F.; L'Huillier, A.; Ferray, M.; Lompré, L. A.; Mainfray, G. Multiple-harmonic generation in rare gases at high laser intensity. *Phys. Rev. A* **1989**, *39* (11), 5751–5761.
- (8) Paul, P. M.; Toma, E. S.; Breger, P.; Mullot, G.; Augé, F.; Balcou, P.; Muller, H. G.; Agostini, P. Observation of a Train of Attosecond

- Pulses from High Harmonic Generation. Science 2001, 292 (5522), 1689–1692.
- (9) Baltuška, A.; Udem, T.; Uiberacker, M.; Hentschel, M.; Goulielmakis, E.; Gohle, C.; Holzwarth, R.; Yakovlev, V. S.; Scrinzi, A.; Hänsch, T. W.; Krausz, F. Attosecond control of electronic processes by intense light fields. *Nature* **2003**, 421 (6923), 611–615.
- (10) Gaumnitz, T.; Jain, A.; Pertot, Y.; Huppert, M.; Jordan, I.; Ardana-Lamas, F.; Wörner, H. J. Streaking of 43-attosecond soft-X-ray pulses generated by a passively CEP-stable mid-infrared driver. *Opt. Express* **2017**, 25 (22), 27506–27518.
- (11) Itatani, J.; Levesque, J.; Zeidler, D.; Niikura, H.; Pépin, H.; Kieffer, J. C.; Corkum, P. B.; Villeneuve, D. M. Tomographic imaging of molecular orbitals. *Nature* **2004**, *4*32 (7019), 867–871.
- (12) Wahlström, C.-G.; Larsson, J.; Persson, A.; Starczewski, T.; Svanberg, S.; Salières, P.; Balcou, P.; L'Huillier, A. High-order harmonic generation in rare gases with an intense short-pulse laser. *Phys. Rev. A* **1993**, *48* (6), 4709–4720.
- (13) Shan, B.; Chang, Z. Dramatic extension of the high-order harmonic cutoff by using a long-wavelength driving field. *Phys. Rev. A* **2001**, *65* (1), No. 011804.
- (14) Corkum, P. B.; Burnett, N. H.; Ivanov, M. Y. Subfemtosecond pulses. *Opt. Lett.* **1994**, *19* (22), 1870–1872.
- (15) Schnürer, M.; Spielmann, C.; Wobrauschek, P.; Streli, C.; Burnett, N. H.; Kan, C.; Ferencz, K.; Koppitsch, R.; Cheng, Z.; Brabec, T.; Krausz, F. Coherent 0.5-keV X-Ray Emission from Helium Driven by a Sub-10-fs Laser. *Phys. Rev. Lett.* **1998**, *80* (15), 3236–3239.
- (16) Zhou, J.; Peatross, J.; Murnane, M. M.; Kapteyn, H. C.; Christov, I. P. Enhanced High-Harmonic Generation Using 25 fs Laser Pulses. *Phys. Rev. Lett.* **1996**, 76 (5), 752–755.
- (17) Ghimire, S.; DiChiara, A. D.; Sistrunk, E.; Agostini, P.; DiMauro, L. F.; Reis, D. A. Observation of high-order harmonic generation in a bulk crystal. *Nat. Phys.* **2011**, *7* (2), 138–141.
- (18) Lakhotia, H.; Kim, H. Y.; Zhan, M.; Hu, S.; Meng, S.; Goulielmakis, E. Laser picoscopy of valence electrons in solids. *Nature* **2020**, 583 (7814), 55–59.
- (19) Luu, T. T.; Garg, M.; Kruchinin, S. Y.; Moulet, A.; Hassan, M. T.; Goulielmakis, E. Extreme ultraviolet high-harmonic spectroscopy of solids. *Nature* **2015**, *521* (7553), 498–502.
- (20) Lanin, A. A.; Stepanov, E. A.; Fedotov, A. B.; Zheltikov, A. M. Mapping the electron band structure by intraband high-harmonic generation in solids. *Optica* **2017**, *4* (5), 516–519.
- (21) Heide, C.; Kobayashi, Y.; Baykusheva, D. R.; Jain, D.; Sobota, J. A.; Hashimoto, M.; Kirchmann, P. S.; Oh, S.; Heinz, T. F.; Reis, D. A.; Ghimire, S. Probing topological phase transitions using high-harmonic generation. *Nat. Photonics* **2022**, *16* (9), 620–624.
- (22) Cox, J. D.; Marini, A.; de Abajo, F. J. G. Plasmon-assisted high-harmonic generation in graphene. *Nat. Commun.* **2017**, *8*, No. 14380. (23) Liu, H.; Li, Y.; You, Y. S.; Ghimire, S.; Heinz, T. F.; Reis, D. A.
- (23) Liu, H.; Li, Y.; You, Y. S.; Ghimire, S.; Heinz, T. F.; Reis, D. A. High-harmonic generation from an atomically thin semiconductor. *Nat. Phys.* **2017**, *13* (3), 262–265.
- (24) Yoshikawa, N.; Tamaya, T.; Tanaka, K. High-harmonic generation in graphene enhanced by elliptically polarized light excitation. *Science* **2017**, *356* (6339), 736–738.
- (25) Yoshikawa, N.; Nagai, K.; Uchida, K.; Takaguchi, Y.; Sasaki, S.; Miyata, Y.; Tanaka, K. Interband resonant high-harmonic generation by valley polarized electron-hole pairs. *Nat. Commun.* **2019**, *10* (1), No. 3709.
- (26) de Vega, S.; Cox, J. D.; Sols, F.; García de Abajo, F. J. Strong-field-driven dynamics and high-harmonic generation in interacting one dimensional systems. *Phys. Rev. Res.* **2020**, 2 (1), No. 013313.
- (27) Alonso Calafell, I.; Rozema, L. A.; Trenti, A.; Bohn, J.; Dias, E. J. C.; Jenke, P. K.; Menghrajani, K. S.; Alcaraz Iranzo, D.; García de Abajo, F. J.; Koppens, F. H. L.; Hendry, E.; Walther, P. High-Harmonic Generation Enhancement with Graphene Heterostructures. *Adv. Opt. Mater.* **2022**, *10* (19), No. 2200715.
- (28) Wang, Y.; Iyikanat, F.; Bai, X.; Hu, X.; Das, S.; Dai, Y.; Zhang, Y.; Du, L.; Li, S.; Lipsanen, H.; García de Abajo, F. J.; Sun, Z. Optical

- Control of High-Harmonic Generation at the Atomic Thickness. *Nano Lett.* **2022**, 22 (21), 8455–8462.
- (29) Nishidome, H.; Nagai, K.; Uchida, K.; Ichinose, Y.; Yomogida, Y.; Miyata, Y.; Tanaka, K.; Yanagi, K. Control of High-Harmonic Generation by Tuning the Electronic Structure and Carrier Injection. *Nano Lett.* **2020**, 20 (8), 6215–6221.
- (30) Kovalev, S.; Hafez, H. A.; Tielrooij, K. J.; Deinert, J. C.; Ilyakov, I.; Awari, N.; Alcaraz, D.; Soundarapandian, K.; Saleta, D.; Germanskiy, S.; Chen, M.; Bawatna, M.; Green, B.; Koppens, F. H. L.; Mittendorff, M.; Bonn, M.; Gensch, M.; Turchinovich, D. Electrical tunability of terahertz nonlinearity in graphene. *Sci. Adv.* **2021**, *7* (15), No. eabf9809.
- (31) Cha, S.; Kim, M.; Kim, Y.; Choi, S.; Kang, S.; Kim, H.; Yoon, S.; Moon, G.; Kim, T.; Lee, Y. W.; Cho, G. Y.; Park, M. J.; Kim, C. J.; Kim, B. J.; Lee, J.; Jo, M.-H.; Kim, J. Gate-tunable quantum pathways of high harmonic generation in graphene. *Nat. Commun.* **2022**, *13* (1), No. 6630.
- (32) Murakami, Y.; Schüler, M. Doping and gap size dependence of high-harmonic generation in graphene: Importance of consistent formulation of light-matter coupling. *Phys. Rev. B* **2022**, *106* (3), No. 035204.
- (33) Garg, M.; Kim, H. Y.; Goulielmakis, E. Ultimate waveform reproducibility of extreme-ultraviolet pulses by high-harmonic generation in quartz. *Nat. Photonics* **2018**, *12* (5), 291–296.
- (34) Vampa, G.; Hammond, T. J.; Taucer, M.; Ding, X.; Ropagnol, X.; Ozaki, T.; Delprat, S.; Chaker, M.; Thiré, N.; Schmidt, B. E.; Légaré, F.; Klug, D. D.; Naumov, A. Y.; Villeneuve, D. M.; Staudte, A.; Corkum, P. B. Strong-field optoelectronics in solids. *Nat. Photonics* **2018**, *12* (8), 465–468.
- (35) Schubert, O.; Hohenleutner, M.; Langer, F.; Urbanek, B.; Lange, C.; Huttner, U.; Golde, D.; Meier, T.; Kira, M.; Koch, S. W.; Huber, R. Sub-cycle control of terahertz high-harmonic generation by dynamical Bloch oscillations. *Nat. Photonics* **2014**, *8* (2), 119–123.
- (36) You, Y. S.; Reis, D. A.; Ghimire, S. Anisotropic high-harmonic generation in bulk crystals. *Nat. Phys.* **2017**, *13* (4), 345–349.
- (37) Shao, C.; Lu, H.; Zhang, X.; Yu, C.; Tohyama, T.; Lu, R. High-Harmonic Generation Approaching the Quantum Critical Point of Strongly Correlated Systems. *Phys. Rev. Lett.* **2022**, *128* (4), No. 047401.
- (38) Murakami, Y.; Uchida, K.; Koga, A.; Tanaka, K.; Werner, P. Anomalous Temperature Dependence of High-Harmonic Generation in Mott Insulators. *Phys. Rev. Lett.* **2022**, *129* (15), No. 157401.
- (39) Uchida, K.; Mattoni, G.; Yonezawa, S.; Nakamura, F.; Maeno, Y.; Tanaka, K. High-Order Harmonic Generation and Its Unconventional Scaling Law in the Mott-Insulating Ca<sub>2</sub>RuO<sub>4</sub>. *Phys. Rev. Lett.* **2022**, *128* (12), No. 127401.
- (40) Nakagawa, K.; Hirori, H.; Sato, S. A.; Tahara, H.; Sekiguchi, F.; Yumoto, G.; Saruyama, M.; Sato, R.; Teranishi, T.; Kanemitsu, Y. Size-controlled quantum dots reveal the impact of intraband transitions on high-order harmonic generation in solids. *Nat. Phys.* **2022**, *18* (8), 874–878.
- (41) Kruchinin, S. Y.; Krausz, F.; Yakovlev, V. S. Colloquium: Strong-field phenomena in periodic systems. *Rev. Mod. Phys.* **2018**, *90* (2), No. 021002.
- (42) Arnold, M. S.; Green, A. A.; Hulvat, J. F.; Stupp, S. I.; Hersam, M. C. Sorting carbon nanotubes by electronic structure using density differentiation. *Nat. Nanotechnol.* **2006**, *1* (1), 60–65.
- (43) Yanagi, K.; Miyata, Y.; Kataura, H. Optical and Conductive Characteristics of Metallic Single-Wall Carbon Nanotubes with Three Basic Colors; Cyan, Magenta, and Yellow. *Appl. Phys. Express* **2008**, *1* (3), No. 034003.
- (44) Yanagi, K.; Udoguchi, H.; Sagitani, S.; Oshima, Y.; Takenobu, T.; Kataura, H.; Ishida, T.; Matsuda, K.; Maniwa, Y. Transport Mechanisms in Metallic and Semiconducting Single-Wall Carbon Nanotube Networks. ACS Nano 2010, 4 (7), 4027–4032.
- (45) He, X.; Gao, W.; Xie, L.; Li, B.; Zhang, Q.; Lei, S.; Robinson, J. M.; Haroz, E. H.; Doorn, S. K.; Wang, W.; Vajtai, R.; Ajayan, P. M.; Adams, W. W.; Hauge, R. H.; Kono, J. Wafer-scale monodomain films

- of spontaneously aligned single-walled carbon nanotubes. *Nat. Nanotechnol.* **2016**, *11* (7), 633–638.
- (46) Komatsu, N.; Nakamura, M.; Ghosh, S.; Kim, D.; Chen, H.; Katagiri, A.; Yomogida, Y.; Gao, W.; Yanagi, K.; Kono, J. Groove-Assisted Global Spontaneous Alignment of Carbon Nanotubes in Vacuum Filtration. *Nano Lett.* **2020**, *20* (4), 2332–2338.
- (47) Fukuhara, K.; Ichinose, Y.; Nishidome, H.; Yomogida, Y.; Katsutani, F.; Komatsu, N.; Gao, W.; Kono, J.; Yanagi, K. Isotropic Seebeck coefficient of aligned single-wall carbon nanotube films. *Appl. Phys. Lett.* **2018**, *113* (24), No. 243105.
- (48) Yanagi, K.; Kanda, S.; Oshima, Y.; Kitamura, Y.; Kawai, H.; Yamamoto, T.; Takenobu, T.; Nakai, Y.; Maniwa, Y. Tuning of the thermoelectric properties of one-dimensional material networks by electric double layer techniques using ionic liquids. *Nano Lett.* **2014**, *14* (11), 6437–6442.
- (49) Igarashi, T.; Kawai, H.; Yanagi, K.; Cuong, N. T.; Okada, S.; Pichler, T. Tuning localized transverse surface plasmon resonance in electricity-selected single-wall carbon nanotubes by electrochemical doping. *Phys. Rev. Lett.* **2015**, *114* (17), No. 176807.
- (50) Yanagi, K.; Okada, R.; Ichinose, Y.; Yomogida, Y.; Katsutani, F.; Gao, W.; Kono, J. Intersubband plasmons in the quantum limit in gated and aligned carbon nanotubes. *Nat. Commun.* **2018**, *9* (1), No. 1121.
- (51) Yomogida, Y.; Pu, J.; Shimotani, H.; Ono, S.; Hotta, S.; Iwasa, Y.; Takenobu, T. Ambipolar Organic Single-Crystal Transistors Based on Ion Gels. *Adv. Mater.* **2012**, *24* (32), 4392–4397.
- (52) Ando, T. Theory of Electronic States and Transport in Carbon Nanotubes. *J. Phys. Soc. Jpn.* **2005**, 74 (3), 777–817.
- (53) Wilhelm, J.; Grössing, P.; Seith, A.; Crewse, J.; Nitsch, M.; Weigl, L.; Schmid, C.; Evers, F. Semiconductor Bloch-equations formalism: Derivation and application to high-harmonic generation from Dirac fermions. *Phys. Rev. B* **2021**, *103* (12), No. 125419.
- (54) Al-Naib, I.; Sipe, J. E.; Dignam, M. M. High harmonic generation in undoped graphene: Interplay of inter- and intraband dynamics. *Phys. Rev. B* **2014**, *90* (24), No. 245423.
- (55) Sato, S. A.; Hirori, H.; Sanari, Y.; Kanemitsu, Y.; Rubio, A. High-order harmonic generation in graphene: Nonlinear coupling of intraband and interband transitions. *Phys. Rev. B* **2021**, *103* (4), No. L041408.
- (56) Keldysh, L. V. Ionization in the field of a strong electromagnetic wave. Sov. Phys. JETP 1965, 20 (5), 1307-1314.
- (57) Ishikawa, K. L. Nonlinear optical response of graphene in time domain. *Phys. Rev. B* **2010**, 82 (20), No. 201402.
- (58) Mikhailov, S. A. Non-linear electromagnetic response of graphene. *Europhys. Lett.* **2007**, *79* (2), 27002.